

RESEARCH ARTICLE

10.1002/2015JC011033

Eddy-topography interactions and the fate of the Persian Gulf Outflow

C. Vic¹, G. Rouillet¹, X. Capet², X. Carton¹, M. J. Molemaker³, and J. Gula¹

Key Points:

- Eddy-topography interactions produce submesoscale coherent vortices (SCVs)
- Background mesoscale eddies in the Gulf of Oman participate to the spreading of Persian Gulf Water
- PGW is spread by small-scale turbulence resulting from eddy-topography interactions

Correspondence to:

C. Vic,
clement.vic@univ-brest.fr

Citation:

Vic, C., G. Rouillet, X. Capet, X. Carton, M. J. Molemaker, and J. Gula (2015), Eddy-topography interactions and the fate of the Persian Gulf Outflow, *J. Geophys. Res. Oceans*, 120, 6700–6717, doi:10.1002/2015JC011033.

Received 8 JUN 2015

Accepted 15 SEP 2015

Accepted article online 21 SEP 2015

Published online 15 OCT 2015

¹Laboratoire de Physique des Océans, UMR 6523, CNRS/Ifremer/IRD/UBO, Brest, France, ²IPSL/LOCEAN, UMR 7159, CNRS/UPMC/IRD/MNHN, Paris, France, ³Department of Atmospheric and Oceanic Sciences, University of California, Los Angeles, California, USA

Abstract The Persian Gulf feeds a warm and salty outflow in the Gulf of Oman (northern Arabian Sea). The salt climatological distribution is relatively smooth in the Gulf of Oman, and the signature of a slope current carrying salty waters is difficult to distinguish hundreds of kilometers past the Strait of Hormuz, in contrast to other outflows of the world ocean. This study focuses on the mechanisms involved in the spreading of Persian Gulf Water (PGW) in the Gulf of Oman, using a regional primitive equation numerical simulation. The authors show that the dispersion of PGW occurs through a regime that is distinct from, for example, the one responsible for the Mediterranean outflow dispersion. The background mesoscale eddy field is energetic and participates actively to the spreading of PGW. Remotely formed eddies propagate into the Gulf of Oman and interact with the topography, leading to submesoscales formation and PGW shedding. Eddy-topography interactions are isolated in idealized simulations and reveal the formation of intense frictional boundary layers, generating submesoscale coherent vortices (SCVs). Interactions take place at depths encompassing the PGW depth, thus SCVs trap PGW and contribute to its redistribution from the boundaries to the interior of the Gulf of Oman. The overall efficiency of these processes is confirmed by a strong contribution of eddy salt fluxes in the interior of the basin, and is quantified using particle statistics. It is found to be a highly dispersive regime, with an approximated eddy diffusivity of $\sim 1700 \text{ m}^2 \text{ s}^{-1}$.

1. Introduction

Dense water outflows are a major component of the Earth climate system. They deliver water masses into the global ocean, whose properties have been transformed in marginal seas. How these waters spread and mix is an important and delicate subject. It involves a series of processes over a wide range of scales that combine their effects in ways unique to each outflow (e.g., review of *Legg et al.* [2009]). While each outflow is different, broad categories can be distinguished. Three of the main outflows, the Mediterranean and Faroe Bank channel outflows and the Denmark Strait overflow, take place in regions with low background eddy activity. In addition, they have a relatively deep equilibrium depth ($>600 \text{ m}$). In these deep and relatively quiescent environments, intrinsic instabilities of the outflows are a fundamental ingredient of their dispersal which takes place over hundreds or thousands of kilometers. An example is the spread of Mediterranean water by Meddies that are generated along the Iberian slope. This outflow regime has been the subject of numerous process studies in the past [e.g., *Griffiths*, 1986; *Price and O'Neil Baringer*, 1994; *Wirth*, 2009]. A different dynamical regime is to be expected when an external source of mesoscale turbulence is present and outflow waters can be passively stirred by mesoscale eddies.

Persian Gulf Water (PGW) is formed in the Persian Gulf and is delivered to the Gulf of Oman through the Strait of Hormuz (see the geographic setting in Figure 1). Initially, it has a large temperature (T) and salinity (S) signature [*Bower et al.*, 2000]. Gulf of Oman climatologies are characterized by subsurface T,S maxima at around 250 m depth where Gulf eddy energy is relatively high, and smooth horizontal T,S gradients around that depth [see *Carton et al.*, 2012, Appendix] and in particular the quasi absence of a T,S signature along the southern Gulf side where PGW would be transported within a continental slope current resulting from the gravitational adjustment of the outflow.

The Persian Gulf Outflow differs from most outflows that it equilibrates at a relatively shallow depth in an energetic environment (located at a western boundary). Figure 2 shows Eddy Available Potential Energy (EAPE) in the three outflow environments mentioned earlier and in the Gulf of Oman. EAPE has been shown

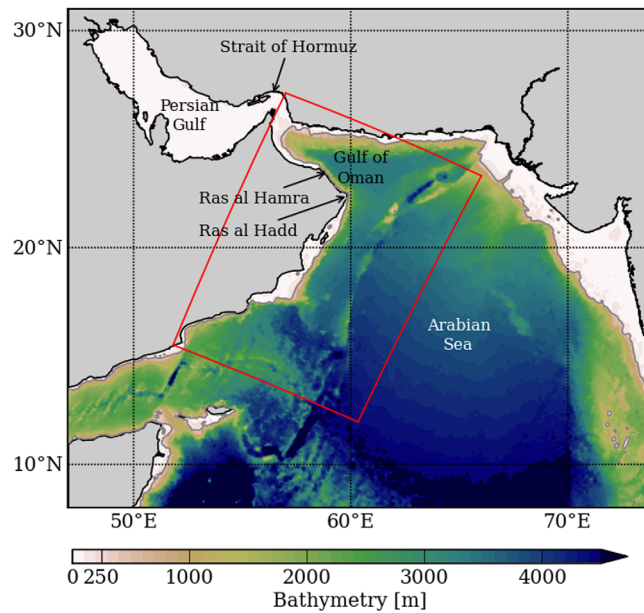


Figure 1. Bathymetry in the Arabian Sea and Persian Gulf derived from ETOPO2 [Smith and Sandwell, 1997]. The red rectangle represents the child domain. The parent domain encompasses the area covered by the map.

to be a good proxy to quantify the intensity of mesoscale turbulence in the ocean interior [Roullet et al., 2014]. It reveals intense eddy activity in the Gulf of Oman around the PGW equilibrium depth (EAPE $\sim 800 \text{ cm}^2 \text{ s}^{-2}$ corresponds to a mean current speed standard deviation, i.e., eddy mean speed, of 40 cm s^{-1}) and confirms that the other outflow regions are quiescent in comparison. Similar to the spread of Red Sea Water in the Gulf of Aden [Ilicak et al., 2011; Bower and Furey, 2012], background mesoscale activity may play an important role in the rapid dispersal of PGW in the Gulf of Oman. Although this has been partially observed in the latter region (using Argo floats in L'Hégaret et al. [2013]), the details of the dispersal phase are unknown.

Surface-intensified mesoscale eddies in the Gulf of Oman have a strong imprint until depths greater than the outflow equilibrium depth (circulation at 700 m depth is highly correlated with the surface circulation) [Carton et al., 2012]. As such, outflow-eddy interactions are to be expected

Surface-intensified mesoscale eddies in the Gulf of Oman have a strong

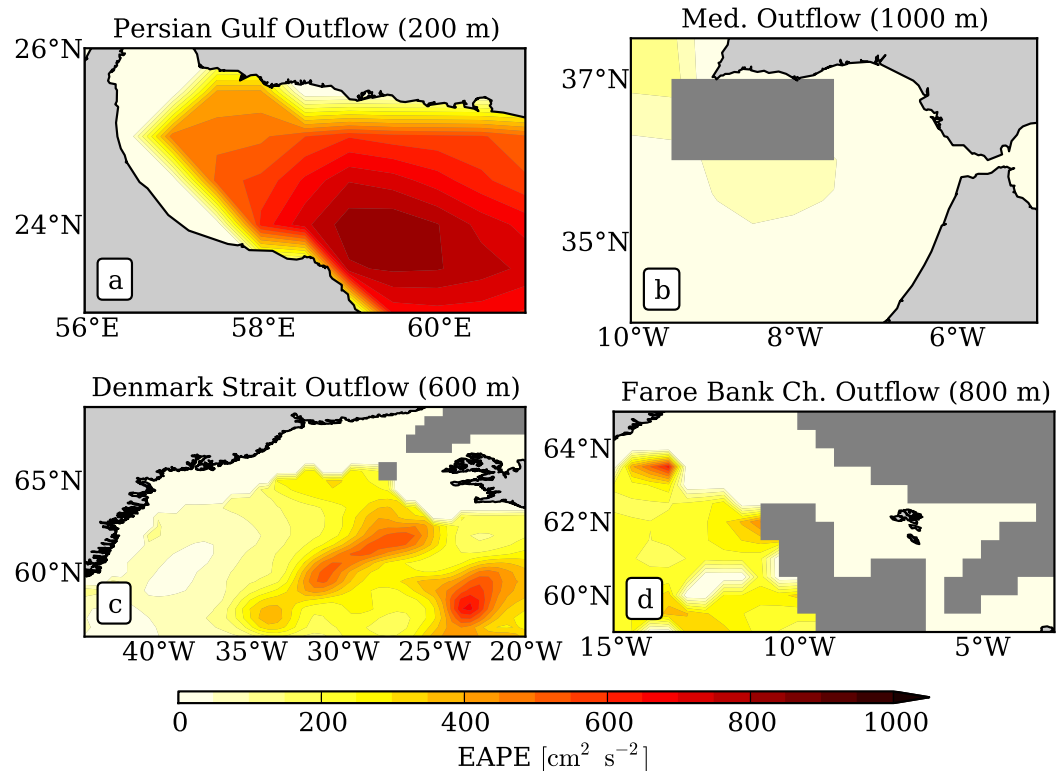


Figure 2. Eddy Available Potential Energy (EAPE) derived from Argo floats (data set described in Roullet et al. [2014]) in (a) the Persian Gulf Outflow environment at 200 m depth, (b) the Mediterranean Outflow environment at 1000 m depth, (c) the Denmark Strait Outflow environment at 600 m, and (d) the Faroe Bank Channel Outflow at 800 m. Depths are chosen to be the equilibrium depths of these outflows following Price and O'Neil Baringer [1994].

[L'Hégaret *et al.*, 2013]. Moreover, the relative narrowness of the Gulf associated with the β -driven westward drift of eddies causes the latter to interact with the topography. Interactions of eddies with topography has received significant attention in idealized contexts. Simplest models with vertical walls as lateral boundaries are useful to study eddy drift, leakage, and decay. A richer variety of processes is present in models with a realistic geomorphology. Noticeably, eddy-topography interactions often produce smaller-scale vortices with an opposite polarity ("bursting" effect) [Robinson, 1991; Akuetevi and Wirth, 2015] and allow the generation of coastally trapped waves [e.g., Sutyryn and Grimshaw, 2010]. An inviscid well-known mechanism involved in the generation of a cyclone when a surface-intensified anticyclone encounters a shelf is the off-shelf advection of waters with high potential vorticity [Frolov *et al.*, 2004; Sutyryn and Grimshaw, 2010]. The resulting eddy is also surface-intensified. In contrast, the viscous response at smaller scales implies the formation of a frictional bottom boundary layer, preferentially on the continental slope. It is found to be a preferred site for strong lateral shears to develop and shear instability to occur, hence generating subsurface vortices [Oey and Zhang, 2004; Molemaker *et al.*, 2015]. We will see that frictional boundary layers play an important role in the dispersion of PGW.

In this study, we describe the spreading of dense PGW beyond the initial phase of gravitational equilibration and investigate the processes at play, using primitive equation numerical simulations. Our results suggest that PGW is efficiently transferred from the boundaries into the Gulf interior where it is rapidly stirred and mixed by mesoscale eddies. In this study, we show that the transfer from the boundaries is the result of sub-mesoscale turbulent structures. Submesoscale turbulence is energized by the interaction of mesoscale eddies with the sloping sides of the Gulf (as opposed to internally generated by the outflow). Thus, both mesoscale and accompanying, frictionally generated, submesoscale eddies conspire to enhance PGW dispersion.

The outline of this paper is as follows. After presenting our investigation tools (section 2), we use the results of a realistic numerical experiment to get phenomenological insight in the dynamics (section 3). We find that PGW is often trapped into submesoscale coherent vortices and that the spread of PGW in the Gulf of Oman may be explained by the cross-Gulf transport of these structures. Idealized numerical experiments, in which the outflow is absent, are presented in section 4. They allow us to confirm that the outflow is not implicated in the formation of the submesoscale vortices. In contrast, they result from the detachment of frictional boundary layers that are found over the continental slope and are associated with mesoscale eddies. In section 5, we assess the efficiency of eddy-topography interactions in diffusing salinity in the Gulf of Oman using both Eulerian and Lagrangian perspectives. Main conclusions of this study are drawn in section 6.

2. Numerical Framework

We use the Regional Oceanic Modelling System (ROMS) [Shchepetkin and McWilliams, 2005] in two different configurations. In the following sections 2.1 and 2.2, we describe the setups used as well as interesting dynamical features in the realistic simulation.

2.1. Realistic Configuration

An off-line one-way nested configuration with a 2 km horizontal resolution is set up from a parent solution described in Vic *et al.* [2014] at 6.6 km resolution. The nesting approach follows the procedure of Mason *et al.* [2010]. The domain is shown in Figure 1. For consistency, the atmospheric forcing is monthly and climatological, identical to the data sets used to force the parent solution [Vic *et al.*, 2014, Table 1]. We use the SCOW climatology of wind stress [Risien and Chelton, 2008] and the ICOADS climatology for heat and freshwater fluxes [Worley *et al.*, 2005]. We changed the bathymetry data set from ETOPO2 [Smith and Sandwell, 1997] to the Shuttle Radar Topography Mission data set (SRTM30-plus) [Becker *et al.*, 2009] for improved spatial resolution (30" instead of 2'). Coordinate parameters and numerical operators are the same as in the parent solution, except for the tracer advection scheme whose diffusive part is rotated along isopycnals for a better conservation of tracer properties [Lemarié *et al.*, 2012]. Open boundary conditions are extracted from the parent solution (years 3–6; the nested configuration was thus run for 4 years) except for the northwestern boundary, situated in the Strait of Hormuz (Figure 1). We carefully tuned the northwestern boundary conditions to have a realistic representation of the outflow properties (barely resolved in the parent solution) using an analytical boundary forcing based on moored Acoustic Doppler Current Profilers (ADCPs)

Table 1. Description of the Sensitivity Tests on Bottom Stress Parameterizations^a

Type	C_D	$\langle \tau \rangle$ ($\times 10^{-3} \text{ N m}^{-2}$)	$\text{std}(u_{\text{bottom}})$ (cm s^{-1})
Linear	$3.0 \times 10^{-4} \text{ m s}^{-1}$	12.4	4.7
Linear	$6.0 \times 10^{-4} \text{ m s}^{-1}$	17.1 (+38%)	3.3 (−30%)
Quadratic	2.5×10^{-3}	8.7	5.1
Quadratic	5.0×10^{-3}	12.2 (+40%)	4.2 (−18%)
Quadratic with Von Karman C_D	Varying	7.9	5.1

^a $\langle \tau \rangle$ is the temporally averaged bottom stress and $\text{std}(u_{\text{bottom}})$ is the standard deviation of the zonal velocity in the bottom layer (we only monitor u because eddy-topography interactions mainly arise in the zonal direction).

and temperature-salinity measurements in the Strait, including a seasonal cycle (measurements described in *Johns et al.* [2003]). This choice deliberately impedes the exploration of intermittent PGW outflow [*Banse, 1997; Thoppil and Hogan, 2009*]. We will see that high-frequency fluctuations in the outflow at the Hormuz Strait are not needed to produce a rich variability downstream.

Figure 3 compares Sea Surface Temperature (SST) and geostrophic EKE of observational data sets with the modeled solution. Although not an extensive evaluation, these comparisons confirm the models ability to produce realistic solutions. The SST snapshots (modeled and from the Moderate Resolution Imaging Spectroradiometer, MODIS) underline comparable variability throughout the domain and very similar frontal features from the coastal upwelling area (Arabian Peninsula) to the north of the domain. In the Gulf of Oman, the presence of a mesoscale eddy is characteristic of the observed dynamics [*e.g., Pous et al., 2004*]. A warm bias is noticeable in the Persian Gulf [*Vic et al., 2014*] but does not affect the nested simulation as the north-western boundary is constructed directly from observational data. EKE is derived from the Absolute Dynamic Topography at $1/4^\circ$ resolution from Aviso. It is found to be slightly higher (by 20% within the domain area) in ROMS although currents have been spatially filtered (Gaussian filtering at 35 km, following *Capet et al.* [2008]) to remove the energy contained in the submesoscale range that is absent in Aviso data.

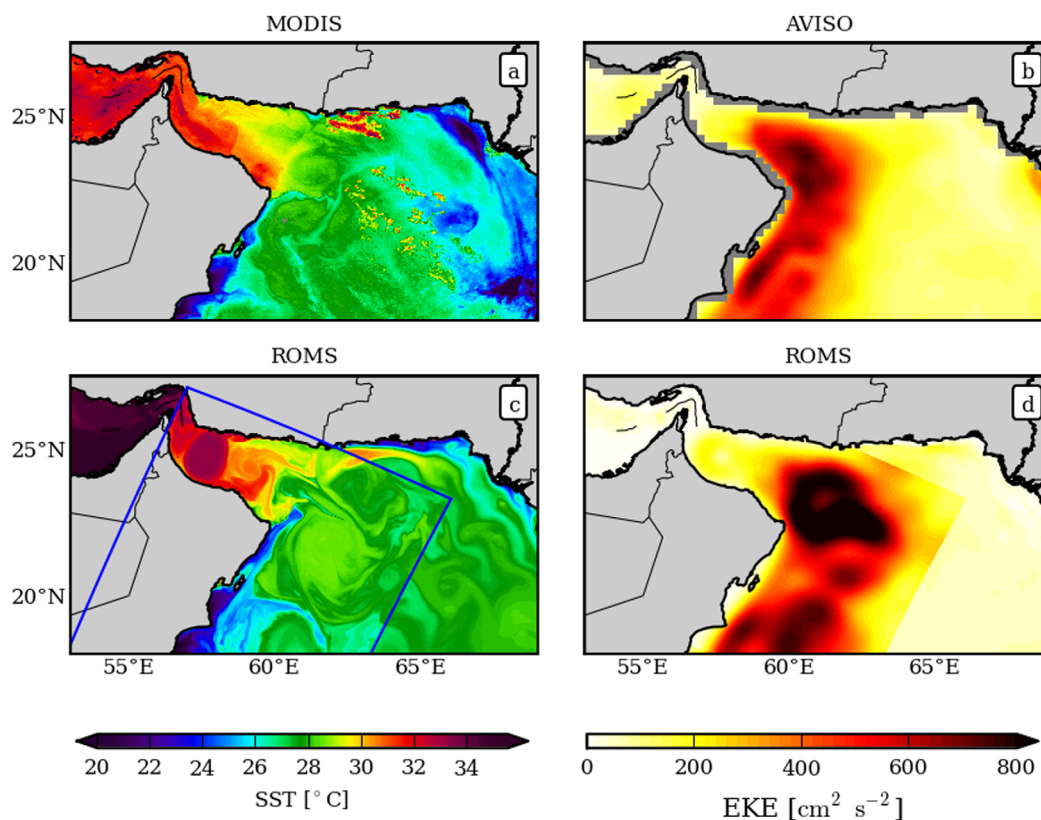


Figure 3. (left) Sea Surface Temperature (SST) from (a) MODIS and (c) the parent and nested (inside the blue rectangle) simulations at for the same period (September). (right) Surface Eddy Kinetic Energy (EKE) derived (b) from Aviso Absolute Dynamic Topography at $1/4^\circ$ resolution and (c) from almost 4 years of simulation. Currents have been low-pass filtered using a Gaussian spatial filter with 35 km half width following *Capet et al.* [2008].

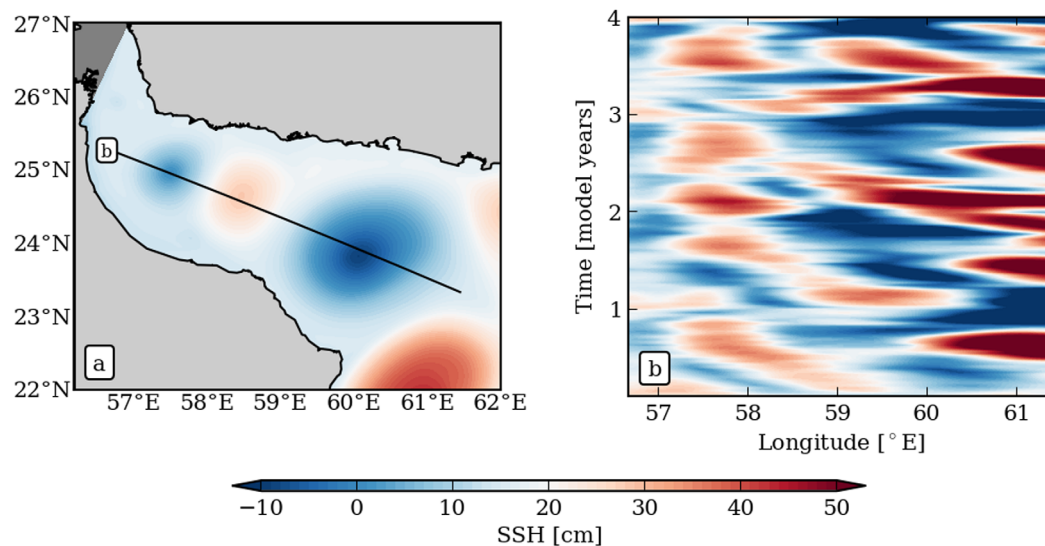


Figure 4. (a) Ten day average map of SSH in the model. (b) Hovmöller diagram of SSH through the 4 years of simulation along the track shown in Figure 4a.

Nonetheless, ranges of variability fit well and confirm that the northwestern Arabian Sea turbulent activity is energetic. The maximum of EKE is situated off Ras al Hadd and is seemingly associated with the seasonal Ras al Hadd jet and surrounding mesoscale eddies [Böhm *et al.*, 1999]. The EKE reduction toward the end of the Gulf is due to the mesoscale eddy decay as they slowly progress westward as we shall see below.

Figure 4a shows Sea Surface Height (SSH) in the Gulf of Oman and reveals a typical situation with several mesoscale eddies present. Their polarity (cyclones and anticyclones are associated with SSH minima and maxima, respectively) alternates here but this is not always the case. Figure 4b reveals the origin of these eddies, coming from the northern Arabian Sea. Once they enter in the Gulf, they are trapped and invariably migrate westward as seen across paths of almost constant SSH. Eddy diameters ($\sim 80\text{--}120$ km) are similar to the full width of the Gulf. As such, the Gulf of Oman acts as an “eddy-guide” for their propagation (a similar situation is found in the Gulf of Aden) [Bower and Furey, 2012]. Mesoscale eddies see their intensity (visible in the amplitude of SSH) decreasing westward. They finally reach the back of the Gulf where they ultimately dissipate, mainly through frictional effects. Cyclones and anticyclones propagate through the Gulf in a chaotic manner, *i.e.*, we could not discern any recurrent pattern. In particular, we found no seasonal preference in polarity. This indicates the fundamentally turbulent nature of the circulation. In the back of the Gulf, around 57.5°E (Figure 4b), there is a tendency for anticyclones to dominate. The time scale for alternating is between 2 and 6 months. This switch has previously been noticed in satellite altimetry (empirical orthogonal function analysis in L’Hégaret [2015]). Hence, by its western position in the Arabian Sea, the Gulf of Oman is continuously forced by remotely formed eddies. Because of the configuration of the Gulf, eddies cannot escape and, as a result, dominate the circulation.

2.2. Idealized Configuration

In order to isolate the interaction of mesoscale eddies with topography, we set up a simplified Gulf of Oman configuration that deliberately omits the outflow. Simplifications also include alongshore invariance of the bathymetry so that flow-topography interactions are easier to analyze. The domain size, the bathymetry profile, and the stratification are realistic (World Ocean Atlas, release 2009). The experiments consist of the free-decay evolution of two horizontally Gaussian-shaped mesoscale eddies that are initially in thermal-wind balance. They are surface-intensified and their kinetic energy vanishes at depth (a similar setup is used in Wei and Wang [2009, Figure 1]). We define each eddy by its center position (x_0, y_0) , its surface temperature anomaly T'_s (no salinity anomaly), its radius R , and its depth range D . We define the temperature field associated with the eddy (prime denotes deviation from the background stratification) as follows:

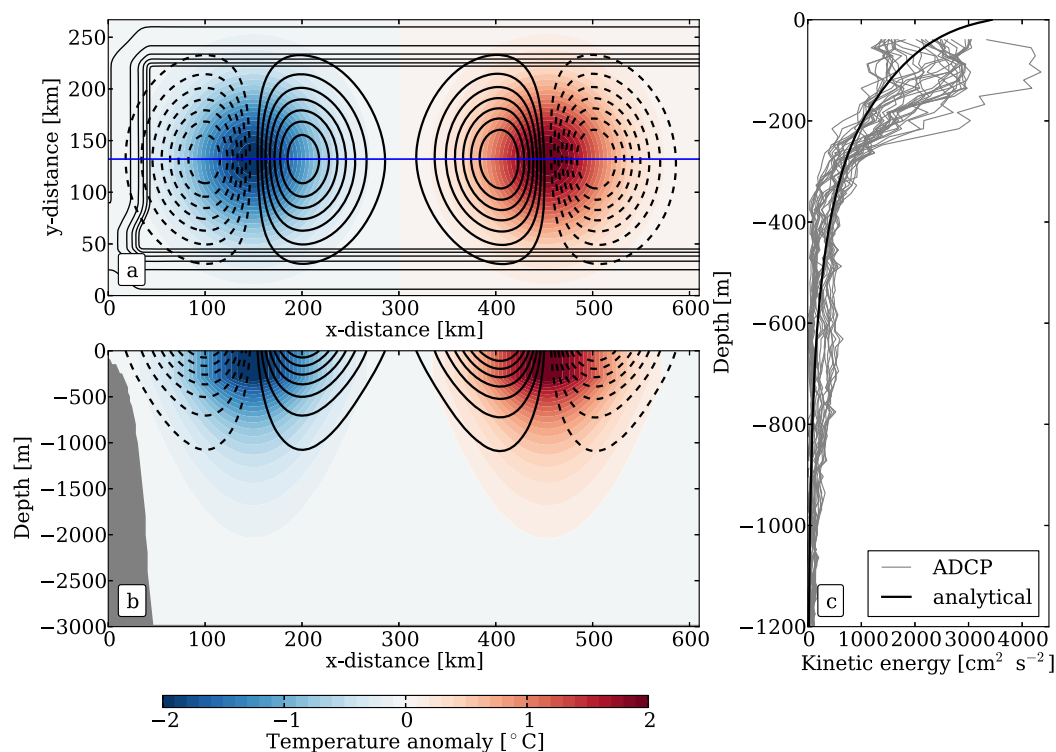


Figure 5. Characteristics of the synthetic cyclone and anticyclone initializing the simulations. Figures 5a and 5b show temperature anomaly (mean vertical background profile has been removed) and contours of meridional velocity from ± 10 to ± 70 cm s^{-1} with $\text{CI} = 10$ cm s^{-1} (dashed lines are negative values). In Figure 5a, thin black lines are contours of bathymetry and the blue line is the location of the section in Figure 5b. Figure 5c shows kinetic energy profiles in the core of the eddies (black thick line) and derived from ADCP measurements in a mesoscale eddy (gray thin lines, Physindien-2011 cruise) [L'Hégaret, 2015].

$$\begin{cases} T'(x, y, z) = T'_s G(x, y), & \text{if } z > \delta \\ T'(x, y, z) = T'_s G(x, y) \exp(-z/D), & \text{if } z < \delta \end{cases} \quad (1)$$

where $G(x, y) = \exp\left(-\frac{(x-x_0)^2 + (y-y_0)^2}{R^2}\right)$ and $\delta = 300$ m. We then compute η (SSH) and (u, v) (horizontal velocity) in two phases. First, we assume that each eddy is isolated and that its associated pressure field does not reach the bottom. Hydrostatic balance integrated over the water column allows us to deduce η . Second, we assume a geostrophic balance to compute the velocity field:

$$\begin{cases} u(x, y, z) = \frac{g}{\rho_0 f} \int_{\eta}^z \partial_y \rho + \underbrace{u(x, y, \eta)}_{=-(g/f)\partial_y \eta} \\ v(x, y, z) = -\frac{g}{\rho_0 f} \int_{\eta}^z \partial_x \rho + \underbrace{v(x, y, \eta)}_{=(g/f)\partial_x \eta} \end{cases} \quad (2)$$

Figures 5a and 5b show horizontal and vertical sections of temperature and anomaly and meridional velocity across the cyclone and the anticyclone. As we are particularly interested in the role of eddies in the Gulf of Oman, we ensure that the vertical structure of simulated eddies in terms of velocity is consistent with local eddies. To do so, we adjust the vertical structure of the temperature anomaly, hence also the velocity profiles of the analytical eddies to match the observations (Figure 5). In fact, we can compare the vertical kinetic energy profiles at the position of the surface velocity maximum for the synthetic eddy and for a mesoscale eddy sampled in the Gulf of Oman during the Physindien-2011 cruise [L'Hégaret, 2015] carried out by the Service Hydrographique et Océanographique de la Marine (SHOM and ADCP measurements). Figure 5c exhibits a fair agreement between the two. It also reveals significant velocities at depth (e.g., 30 cm s^{-1} at 500 m). After migrating westward due to beta drift, the eddy evolution is governed by mutual interaction and topographic influence.

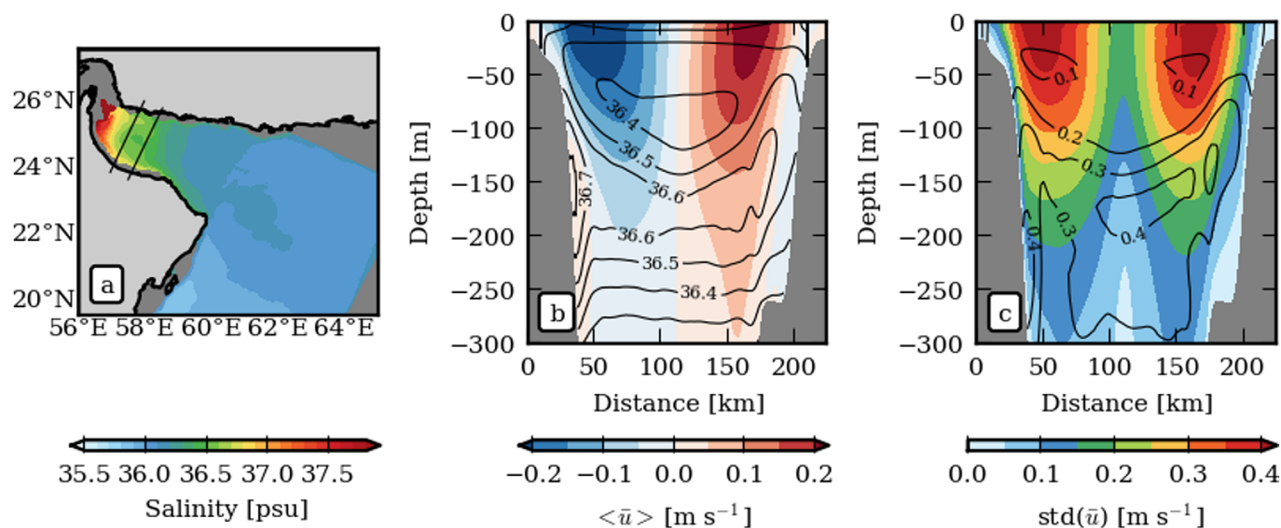


Figure 6. (a) Map of salinity averaged in time (4 years) and vertically between 100 and 250 m. (b, c) Vertical sections of along-gulf velocity (colors) and salinity (black contours) averaged in the along-gulf direction between the two thin black lines in Figure 6a. Figure 6b are time means (4 years) and Figure 6c are standard deviations (biased estimator).

3. Phenomenology

In this section, we analyze the fate of the modeled outflow in the realistic simulation.

3.1. Mean Structure

The dense PGW cascades down the continental shelf break (~ 100 km downstream from the Strait, Figure 1). We do not analyze this phase, which involves small-scale turbulence processes that are not properly represented in our model. The outflow reaches a depth of equal density at which point the flow is hydrostatic and geostrophically balanced, and the outflow establishes itself with the coast on its right, as expected from a density current in the northern hemisphere. Figure 6a shows salinity averaged during the 4 years of simulation between 100 and 250 m. It reveals a salty plume with a maximum located on the right of the Gulf close to the Strait of Hormuz but there is no significant variation of salinity across the Gulf further away. This plume morphology is also found in observations [Carton *et al.*, 2012]. Figure 6b shows salinity and along-gulf velocity averaged in the along-gulf direction and in time ($\bar{\cdot}$ is an along-gulf average and $\langle \cdot \rangle$ is a time average). Figure 6c is the same for standard deviations. The dominant signal is the dipolar velocity structure corresponding to a surface-intensified eddy with a diameter of ~ 100 km. After 4 years of averaging, the remaining polarity is anticyclonic, corresponding to a slight dominance of positive SSH at this longitude in Figure 4. However, the standard deviation dominates the mean, consistent with the alternating presence of cyclones and anticyclones.

The salinity local maximum hugs the coast and is associated with a maximum in velocity. This gravity current is characterized by a mean speed of $\langle \bar{u} \rangle \sim 0.05\text{--}0.1$ m s⁻¹, comparable to the Nof's [1983] speed $u_g = g'\alpha/f = 0.13$ m s⁻¹, where g' is the reduced gravity and α is the slope of topography evaluated using the section shown in Figure 6b. Note that the Nof speed does not account for frictional processes which may explain the discrepancy. The mean salinity of the current is $\langle \bar{S} \rangle \sim 36.8$ psu (slightly less than synoptic measurements, 37 psu) [Pous *et al.*, 2004]. The level of equilibration of PGW (100–250 m) is also slightly shallower than observed (150–300 m) [Pous *et al.*, 2004]. We attribute this to the imperfect representation of the frictional Ekman bottom layer (the downslope movement of density currents is strongly constrained by the vertical resolution at depth) [Laania *et al.*, 2010] and gravitational adjustment as a whole is a difficult process to reproduce [Peters *et al.*, 2005]. As in the observations [Carton *et al.*, 2012], the mean salinity distribution is smooth, in particular in the cross-Gulf direction, with maximum salinity values located between 100 and 250 m throughout the gulf. There are two maxima in salt variability that are located in the slope current and in the interior ($\text{std}(\bar{S}) = 0.4$ psu). This suggests that the slope current, bringing saline waters, displays a strong temporal variability and that saline water may be injected in the inner basin. This is supported by the weak imprint of the density current. Salinity at the boundary is only 0.3 psu higher than in the interior. For comparison, salinity contrast for the Mediterranean outflow is larger than 0.6 psu [Legg *et al.*, 2009].

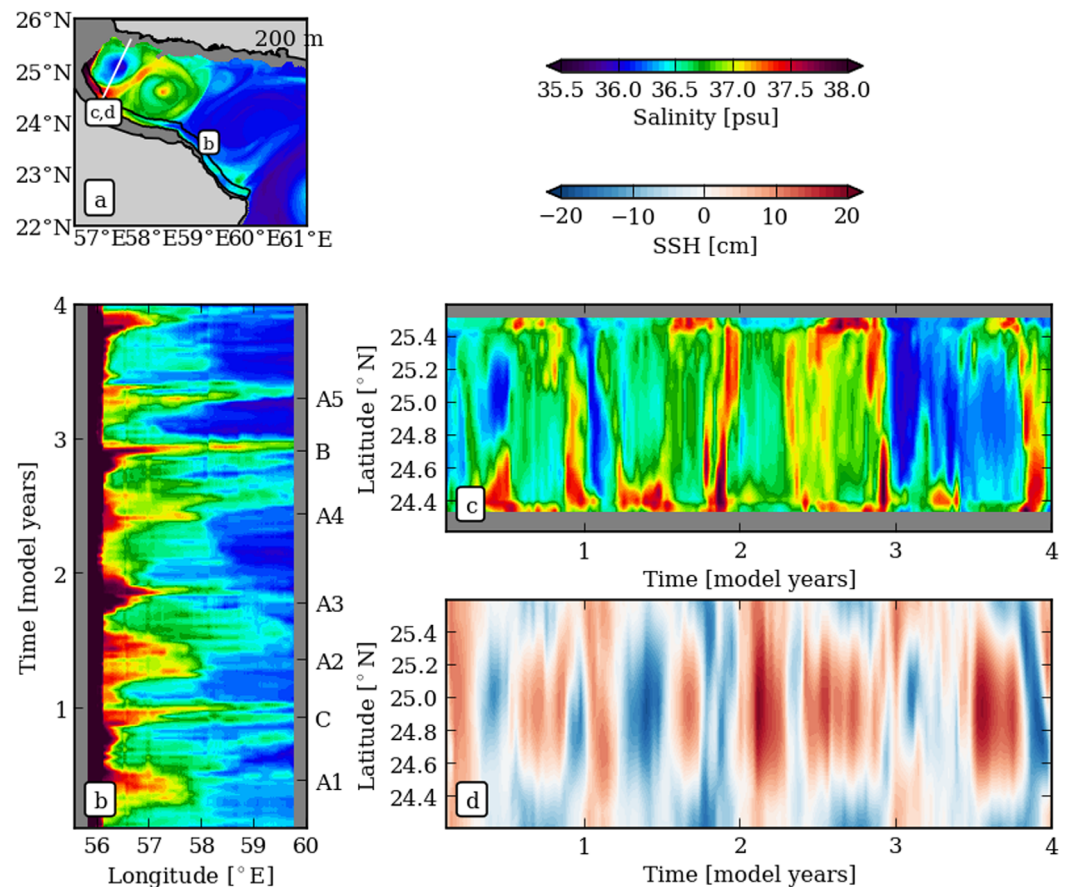


Figure 7. (a) Salinity map at 200 m averaged on 10 days. (b) Longitude-time diagram of salinity (depth averaged between 100 and 250 m and cross-shore integrated from the coastline to 20 km offshore) along the path of PGW delimited by black lines in Figure 7a. (c, d) Latitude-time diagram of salinity (depth averaged between 100 and 250 m) and sea surface height, respectively, at the section shown as white line in Figure 7a.

The mean salinity structure in the far field (downstream from Ras al Hamra, Figure 1) exhibits a very low imprint of PGW (anomalies are less than 0.1 psu) and there is no imprint of a density current. This supports that PGW has been almost completely diluted at this location.

3.2. Intermittency of the Slope Current

Figure 7 makes use of the 4 years of simulation to quantify the salinity distribution evolution in the Gulf of Oman. Salinity in Figure 7b is depth averaged between 100 and 250 m and cross-shore integrated over a 20 km wide strip ($\sim R_d/2$, typical of the slope current width, R_d being the deformation radius). Salinity in Figure 7c is depth averaged between 100 and 250 m. These figures illustrate the spatiotemporal variability of the salt content in the PGW current (Figure 7b) and through a cross-basin section (Figure 7c). The southern filament (that may be associated with the slope current) exhibits a very strong intermittence: salinity in the coastal range, upstream of Ras al Hamra (longitude $< 58.5^\circ\text{E}$), varies between 36 and 38 psu. Values above 37 psu are characteristic of PGW [Pous *et al.*, 2004] and peak approximately twice a year. This is not related to the boundary forcing as the seasonal variability in salinity is weak (maximum is always above at 39.5 psu). It thus has to be the result of another process, which is the intermittent interaction of the coastal undercurrent with the mesoscale eddy field.

Figure 7d shows SSH on the same line as the section in Figure 7c. Latitude-time diagrams (Figures 7c and 7d) show the alternating presence of PGW along the northern (resp. southern) coast depending on whether an anticyclone (resp. a cyclone) occupies the end of the Gulf. This strongly suggests a steering of PGW by mesoscale turbulence. Similar latitude-time diagrams at locations downstream of Ras al Hamra (not shown) reveal the same steering of PGW, and very diluted waters (salinity ~ 36.1 psu) occasionally reaching the Gulf

entrance. This variability in outflowing water paths driven by mesoscale eddies is similar to the fate of the Red Sea Water outflowing in the Gulf of Aden [Ilicak *et al.*, 2011].

A close examination of the salinity field at a temporal resolution of 12 h allows to focus on some particular events. Events labeled A_i ($i \in 1 \dots 5$, Figure 7b) correspond to detachments of PGW from the southern coast propagating into the interior (dynamical characteristics are discussed in the next section 3.3). They are associated with the presence of a cyclone that seemingly sheds the saline water seaward. Similar events occur on the northern coast when an anticyclone lies at the back of the Gulf. These events break the slope current, expel PGW seaward, and efficiently redistribute PGW into the basin interior (in coherence with the salinity standard deviation maximum in the interior in Figure 6). They are season-lasting events, relying on surface-intensified eddies to imprint their dynamics at depth. Hence, they provide a hint of explanation for horizontally isotropic plumes of PGW seen on climatological fields in the Gulf of Oman. Events labeled B and C (also in Figure 7c), respectively, correspond to a “reattachment” and a flush of PGW. They are characterized by a salinity maximum at the southern boundary corresponding to a continuous saline filament heading to the entrance of the Gulf. These events are rarely observed and the slope current is almost always discontinuous.

3.3. Submesoscale Coherent Vortices Contain PGW

The realistic simulation shows a rich diversity of situations in terms of PGW distribution and turbulent features containing PGW. Figure 8 presents a typical event (from the family of events A_i in Figure 7 identified above) occurring in the simulation that helps to understand this spread. A cyclone fills the Gulf of Oman downstream of Ras al Hamra. It can be identified by means of a positive core of vertical relative vorticity ($\zeta = \partial_x v - \partial_y u \sim 0.5f$, (u, v) is the horizontal velocity) and a maximum in density (Figures 8a and 8b). The mean radius of deformation in this region is $R_d = 41$ km and the eddy diameter is 120 km $\sim 3 R_d$, i.e., in the mesoscale range. The cyclone is energetic with a maximum velocity at 200 m of 0.5 m s^{-1} . Its deep-reaching flow field (isopycnal tilts reach 1000 m) is consistent with Carton *et al.* [2012], who showed a strong correlation between a float trajectory at 700 m and geostrophic surface circulation derived from altimetry.

Around the rim of the cyclone, five small patches of negative vorticity are present. They correspond to Submesoscale Coherent Vortices (SCV) [McWilliams, 1985] with horizontal length scales less than R_d (between $R_d/2$ and R_d). Their vertical extension is consistent with that of the *Peddy* (standing for *Persian Gulf Eddy*, similarly to *Meddy*) sampled by Senjyu *et al.* [1998]. The SCV core vorticity reaches $O(-f)$, consistent with the high intensity of such submesoscale structures. Embedded within the SCVs are anomalously high values of salinity (Figures 8c and 8f), hence revealing PGW. The core of PGW in this section is shallower than its mean because it is contained into a mesoscale cyclonic structure, thus having tilted isopycnals upward (this vertical shift of PGW position depending on the polarity of the structure has been noticed in cruise and Argo floats observations in L'Hégaret *et al.* [2015]). Interestingly, at the period of formation of the SCV (Figure 8f), there is no exact colocalization of the hydrological (salinity) and dynamical (vorticity) cores. In fact, the patch of positive anomaly of salinity is more diffuse horizontally and vertically than the vorticity core. To confirm the robustness of this visual feature, we compute the Probability Density Functions (PDFs) of the depth of relative vorticity maximum and the depth of salinity maximum through all water columns in an area covering the Gulf of Oman, during a period of 20 days encompassing the snapshot in Figure 8 (see the caption of Figure 9 for details on the computation). PDFs in Figure 9 show that the vorticity maximum is found around 125–150 m (we investigate the processes responsible for this subsurface vorticity maximum in section 4) whereas the salinity maximum have mainly three distinct peaks, between 100 and 275 m, depending on the location of PGW (in fact, a shift in PGW depth is noticed whether it is embedded in a cyclone or an anticyclone, and PGW core also deepens downstream from the Strait). Indeed, vorticity and PGW cores are seemingly decorrelated. This is a clue to infer on the passive role of the slope current in the formation of SCVs (further arguments on spatiotemporal scales involved are discussed in section 4.2). Instability of the current would have led to a colocalization of hydrological and dynamical cores (e.g., saline Levantine Intermediate Water spread through SCVs generated by an undercurrent detachment) [Bosse *et al.*, 2015].

The coherence of the structures ($\zeta/f \sim -1$) allows to infer a mechanism of transport of PGW seaward as entrained in a rotation around the central mesoscale eddy (see velocity field in Figure 8d). This kind of

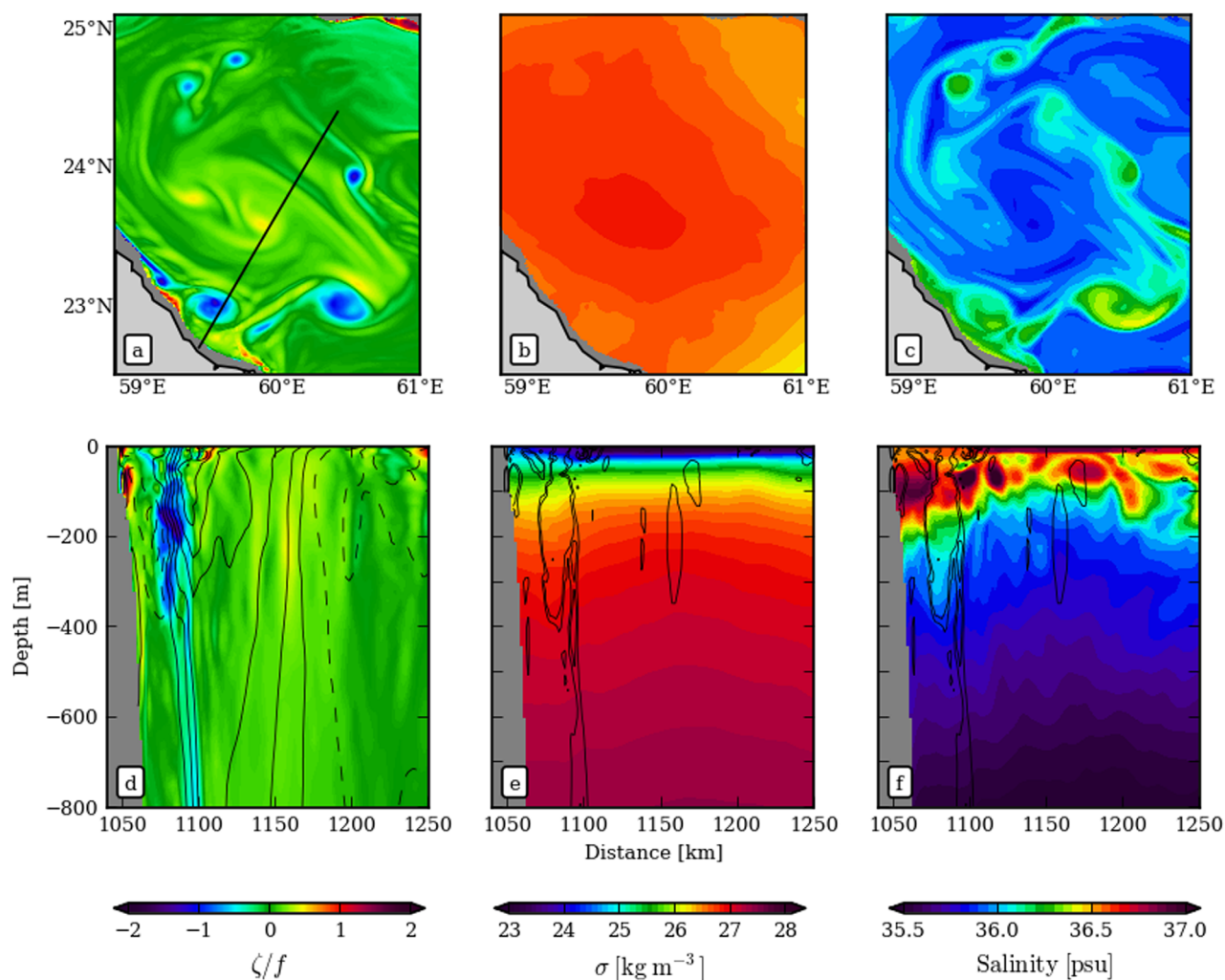


Figure 8. (top) Maps at 200 m and (bottom) sections of (left) relative vorticity ζ nondimensionalized by the planetary vorticity f , (middle) density, and (right) salinity. The black line in Figure 8a is the location of the sections. Black contours in Figure 8d are cross-section velocity ranging from -0.5 to 0.5 m s^{-1} with $\text{CI} = 0.1 \text{ m s}^{-1}$ (negative values are dashed). Black contours in Figures 8e and 8f are ζ/f ($\pm 0.4, 0.6$).

trajectory has been reported with a mode water SCV around a mesoscale anticyclone in the Atlantic [Reverdin *et al.*, 2009]. However, SCVs in the model rapidly collapse and coherent structures cannot be tracked longer than 10 days in the simulation. We attribute this short life cycle to the strong deformation field (shear s and strain σ) in the vicinity of mesoscale eddies (Figure 10). In fact, although we have $s, \sigma < \zeta$ in SCVs (confirming their coherence as rotating structures), the magnitude of the mesoscale shear and strain is comparable with SCV vorticity values. As such, they compete with it and tend to damage the submesoscale structures.

4. Processes at Play

In this section, we evidence how the kind of SCVs described previously can arise from interactions of mesoscale eddies with topography. We did several idealized experiments and present the most interesting results.

4.1. Vorticity Production on the Slope

Figure 11 shows maps and a section of relative vorticity for a snapshot of an idealized experiment. We recall that the experiment is initialized with two opposite polarity mesoscale eddies representative of the ones encountered in the Gulf of Oman. At the surface, the dominant feature is thus the mesoscale dipole with

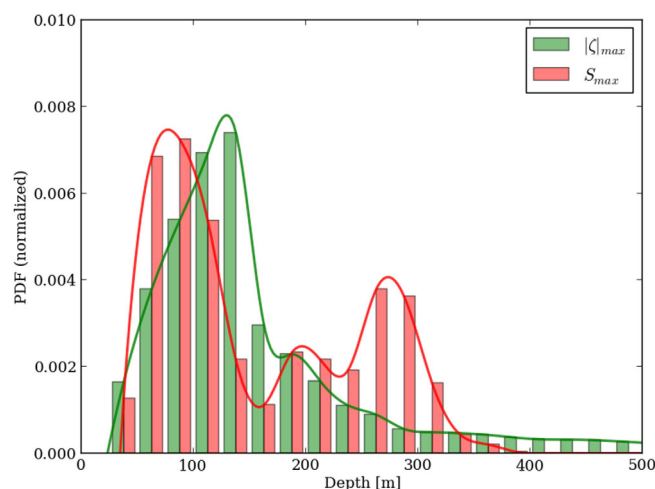


Figure 9. Probability density functions (PDFs) of the depth of (green histogram) relative vorticity maximum $|\zeta|_{\max}$ and (red histogram) salinity maximum S_{\max} computed on 20 days around snapshot in Figure 8, in an area covering the Gulf of Oman (between vertices 23.8°N, 56.6°E; 26.5°N, 57.8°E; 25.2°N, 61.2°E; 22.5°N, 59.7°E). Depth is binned from 25 to 800 m with a constant bin width of 25 m (x axis is cut at 500 m). Lines are cubic splines interpolations between histogram rectangles.

ity intensity depends on the width of the frictional layer. Vorticity strips are shed from the continental slope at the edge of their “parent” mesoscale eddies and suddenly roll up into SCVs (Figure 11b, $x \sim 350$ km). Instability of those vorticity strips carrying horizontal velocity shears is discussed in section 4.2. Notice that we characterize these vortices as submesoscales as their diameters are in the range ~ 35 – 40 km, thus slightly less or comparable to R_d .

Similar processes are discussed in *D’Asaro* [1988] and *Molemaker et al.* [2015] of the formation of a frictional boundary layer at depth. A key difference here is that friction acts on mesoscale eddy velocities instead of a boundary current (upwelling undercurrent for instance). Another difference is that detachment does not require a topographic irregularity like a cape or a canyon. Here rotation of the flow around mesoscale structures implies that currents are in some places oriented across the continental slope which promotes detachment, in the same fashion as in *Oey and Zhang* [2004] and *Akuetevi and Wirth* [2015]. Among the eddy-topography interaction processes described in the introduction, the dominating one in our simulation is thus the frictional formation of boundary layers and the relaxation of smaller-scale eddies.

To test the hypotheses that vorticity is produced: (i) on the continental slope, and (ii) due to bottom friction (the model vertical boundary layer implies a horizontal shear layer [*Molemaker et al.*, 2015, Figure 7]), we ran two experiments with and without bottom stress. We use a linear bottom stress with a drag coefficient $C_D^{\text{lin}} = 3 \cdot 10^{-4} \text{ m s}^{-1}$ (similar to what is commonly used) [e.g., *Dong et al.*, 2007]. Sensitivity to the bottom stress parameterization is tested in the next section 4.2. Figures 12a and 12b present the enstrophy horizontal spectra $\zeta^2/2$ as a function of depth for both experiments, computed on the same rectangular box ($x \in [46 \text{ km}; 457 \text{ km}]$, $y \in [49 \text{ km}; 217 \text{ km}]$) and averaged over the same period (between days 45 and 75 to allow for the eddies to interact with the topography while keeping a sufficient level of energy because the system is freely decaying). The global picture matches what is expected from geostrophic turbulence in the ocean: enstrophy is mostly contained in surface-intensified structures with a scale of 2 – $3 R_d$ (mesoscale eddies in this case) and vanishes with depth at a given wave number. Looking more specifically at isoline -7 in Figure 12a reveals a positive anomaly of enstrophy between 200 and 800 m. An interior source of enstrophy at scales smaller than or equal to R_d is thus located on the continental slope. The simulation without bottom stress does not exhibit the same enstrophy creation at depth (Figure 12b). Moreover, neither frictional boundary layer nor SCV are observed, in agreement with similar experiments carried out in *Oey and Zhang* [2004]. Enstrophy is monotonically decreasing with depth for all wave numbers. The ratio of the two enstrophy power density spectra quantifies this fundamental difference to be an order of magnitude greater (Figure 12c) and validate hypotheses (i) and (ii).

core vorticity values of $\sim \pm 0.5f$ (similar to the ones realistically simulated). At depth, the footprint of the dipole is noticeable and each mesoscale eddy is surrounded by some smaller eddies of opposite polarity whose sizes ($\leq R_d$) and vorticity amplitudes ($|\zeta/f| \sim 1$) are typical of SCVs. Note that these SCVs exist in a subsurface layer and have no surface signature.

Below 150 m, a very thin layer of high vorticity $|\zeta/f| > 1$ develops where mesoscale eddies encounter the continental slope. Vorticity in the boundary layer has an opposed polarity to the eddy dragging on the slope. It is generated as the velocity field slows down toward the shore due to friction in the boundary layer. Vorticity would probably be even larger in a higher-resolution simulation as found in *Molemaker et al.* [2015] because the vortic-

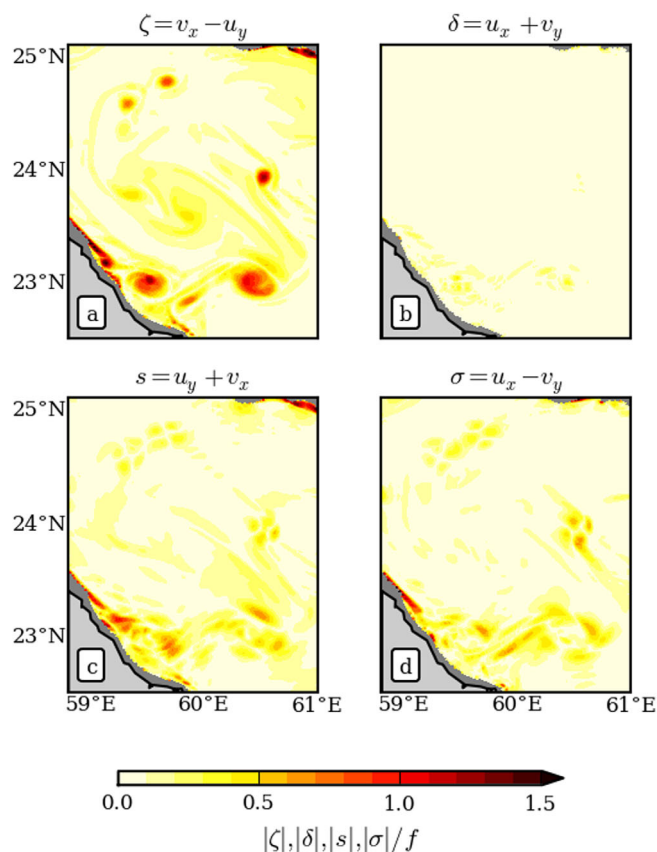


Figure 10. Maps at 200 m of the absolute value of (a) relative vorticity $|\zeta|/f$, (b) divergence $|\delta|/f$, (c) shear $|s|/f$, and (d) strain $|\sigma|/f$. All fields are computed at the same time, identical to Figure 8.

simulation does no justice to the details of evolving centrifugal instability and subsequent mixing of momentum due to the limitations of resolution and the hydrostatic assumption, the flow does quickly adjust to a state that is subcritical. Negative vorticity values that are lower than $-f$ are routinely generated in frictional boundary layers. These values are diluted to satisfy $\zeta > -f$ as soon as vorticity strips detach from the stabilizing continental slope. We argue that the same mechanism occurs in our simulations when a mesoscale cyclone drags on the continental slope and generates anticyclonic SCVs (Figure 8).

The cyclonic case has been studied on the cyclonic side of the Gulf Stream at the exit of the Florida Strait [Gula et al., 2015]. The Gulf Stream drags on the continental slope on its left, generating positive vorticity by friction. After separation of the flow from the slope, the vorticity filament becomes unstable and rolls up into a string of cyclonic submesoscale vortices. Gula et al. [2015] show that barotropic instability, thus linked with the instability of a horizontal shear flow, is the main process generating those vortices.

Another potential candidate for the generation of eddies in the realistic simulation could be the baroclinic instability of the slope current [Griffiths, 1986]. The linear stability analysis of a slope current [Stephens, 1997] applied to the intermittent slope current in our simulation gives a maximum growth rate of $\sim 0.12 U/R_d$ corresponding to a wavelength of $\sim 2\pi R_d/0.7$ (using a continental slope of 0.02, mean value upstream Ras al Hamra). With a slope current that reaches $U \sim 0.3 \text{ m s}^{-1}$ and $R_d = 41 \text{ km}$, this gives a growth rate of $1/13 \text{ days}^{-1}$ and a wavelength of 360 km. These spatiotemporal scales are incompatible with SCVs and we therefore reject this as a generation mechanism of SVCs.

4.3. Sensitivity to the Bottom Stress Parameterization

The development of frictional layers in the simulations occurs when an eddy drags on the bottom slope. The strength of the friction depends on how the bottom stress τ_b is parameterized in ROMS. We are able to use either a linear bottom stress $\tau_b = \rho_0 C_D^{lin} \mathbf{u}$ or a quadratic bottom stress $\tau_b = \rho_0 C_D^{quad} \|\mathbf{u}\| \mathbf{u}$ where ρ_0 is a

4.2. Generation of SCVs

We observe both cyclonic and anticyclonic SCVs in the realistic (although not precisely quantified, we observe a slight preference for anticyclones) and in the idealized simulations. The polarity of an SCV is opposed to the polarity of its *parent* mesoscale eddy that has dragged on the slope. Mechanisms leading to the formation of vortical structures emerging from intense frictional boundary layers was first observed by D'Asaro [1988] and has recently been revisited using high-resolution models [Dewar et al., 2015; Gula et al., 2015; Molemaker et al., 2015]. They involve different instability processes depending on the polarity of the boundary layer.

The case of anticyclonic boundary layers has been studied in the context of the California Undercurrent [Molemaker et al., 2015; Dewar et al., 2015]. Flowing poleward along the US West Coast, it generates negative vorticity in the boundary layer. With a sufficient resolution, vorticity in the boundary layer becomes larger than f and instigates centrifugal instability when the flow separates from the slope. While our sim-

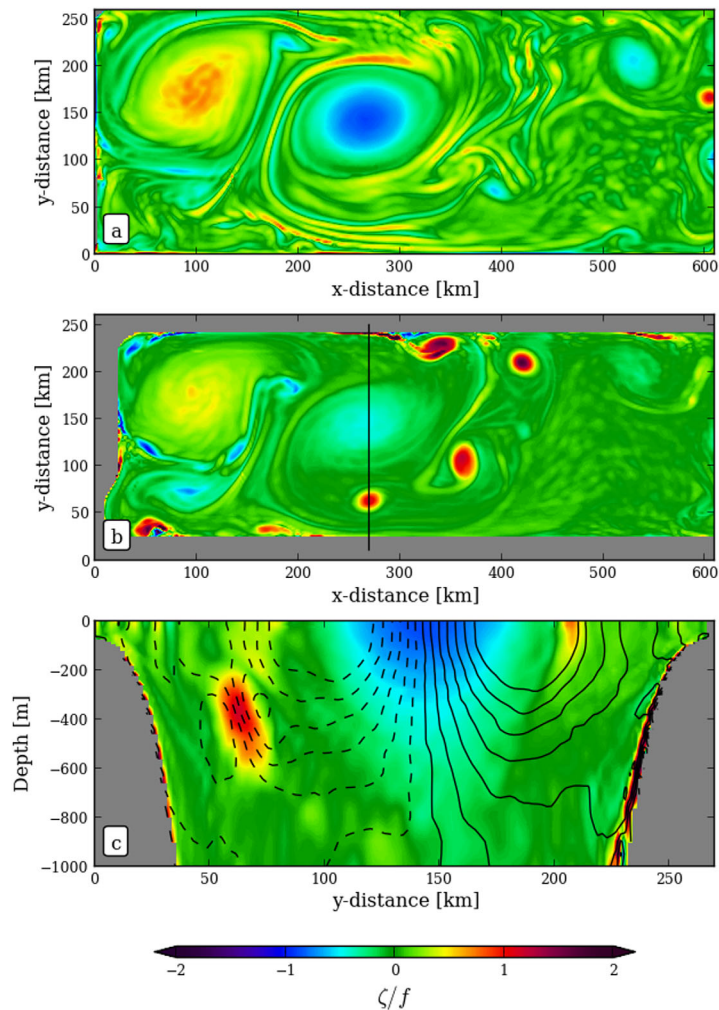


Figure 11. Snapshot maps and section of relative vorticity ζ/f in the idealized experiment with linear bottom stress. Maps are (a) at the surface and (b) at 400 m. Black line in Figure 11b indicates location of section in Figure 11c. Black contours in Figure 11c are cross-section velocity ranging from -0.6 to 0.6 m s^{-1} with $\text{CI} = 0.1 \text{ m s}^{-1}$ (negative values are dashed).

reference density, C_D is a drag coefficient, and \mathbf{u} is the horizontal velocity. In the linear formulation, C_D is constant. In the quadratic formulation, it can be constant or vary with the thickness of the lowest layer of the grid Δz_b . This uses the Von Karman-Prandtl logarithmic formulation $C_D^{\text{VonKarman}} = \left(\frac{\kappa}{\log(\Delta z_b/z_r)} \right)^2$ where $\kappa = 0.41$ is the Von Karman constant and z_r is the roughness parameter usually taken in the range $O(10^{-2} - 10^{-3} \text{ m})$.

We made several simulations with linear and quadratic bottom stresses and varying C_D . Experiments are described in Table 1. The first observation we made is that neither the nature of the parameterization (linear or quadratic) nor the value of C_D changes qualitatively the eddy-topography interactions. Formation of frictional boundary layers is still present and roll-up of vorticity strips into vortices in the interior occurs as soon as a drag is parameterized. The evolution of the bottom stress is very similar in all cases (Figure 13). A peak occurs at the beginning of the simulation when the velocity field is dramatically damped in the bottom level (initialization does not take into account a reduction of velocity in the bottom level). Then the bottom stress decreases and fluctuates around its mean value from day 20 onward. An interesting point is that the mean bottom stress increases with C_D (Table 1) but with a smaller rate: doubling C_D only increases $\langle \|\tau\| \rangle$ by 38% (linear case) and 40% (quadratic case). It also reduces the bottom layer velocity standard deviation $\text{std}(u_{\text{bottom}})$ by comparable factors. This suggests that the bottom stress is not very sensitive to the drag coefficient itself. The Von Karman formulation of the drag coefficient does not really impact the bottom stress

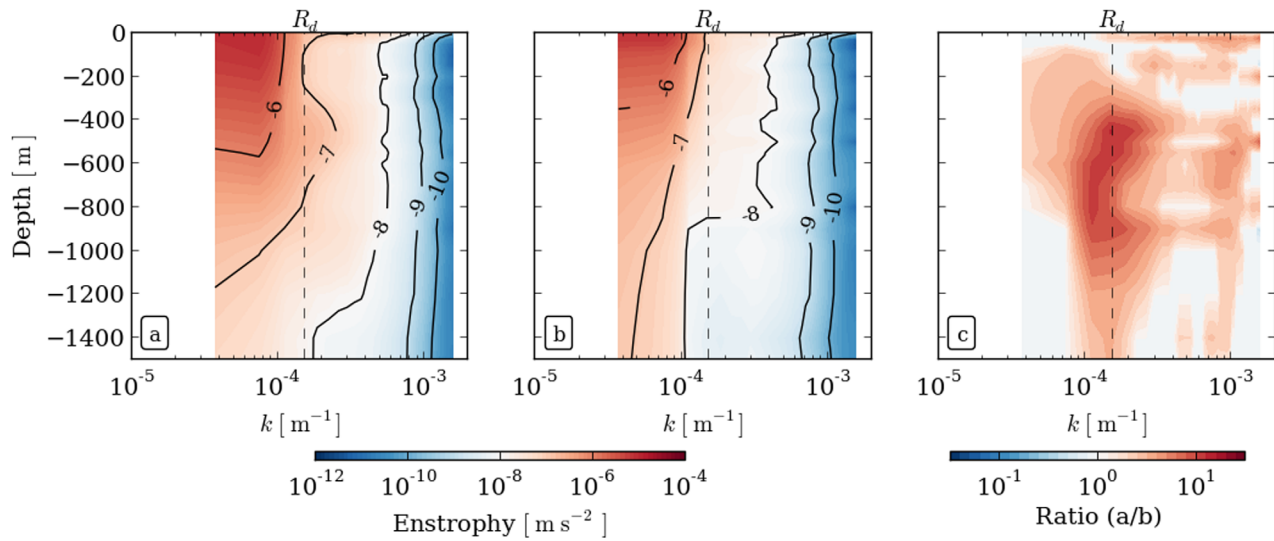


Figure 12. Entrophy spectral density as a function of depth averaged over 1 month in the idealized experiments (a) with linear bottom stress and (b) with no bottom stress. Figure 12c is the ratio of (a)/(b). $k = (k_x^2 + k_y^2)^{1/2}$ is the horizontal wave number. The vertical dashed line shows the deformation radius scale (R_d).

and its integrated value is very similar to the quadratic case with $C_D = 2.5 \cdot 10^{-3}$ (Figure 13). This is not surprising since the bottom stress mainly acts around 400 m (see the large vorticity values in Figure 3 of the manuscript) and $C_D^{VonKarman} (\sim 400 \text{ m}) \sim 2-4 \cdot 10^{-3}$. This more sophisticated formulation does not really bring changes in the simulations here.

To conclude, we can state that the velocity field is not sensitive to the bottom stress formulation and the drag coefficient used in our simulations. All sensitivity tests exhibit similar eddy-topography interactions, thus the phenomenology described in the manuscript is robust.

5. Turbulent Diffusion

In this section, we assess the efficiency of eddy-topography interactions described previously in diffusing the salinity in the Gulf of Oman.

5.1. Eulerian Perspective

We start with an Eulerian point of view that reveals the significance of eddy fluxes in distributing salinity in the Gulf. We separate the contributions of salt fluxes into a mean and an eddy part:

$$\nabla_{3D} \cdot \overline{uS} = \nabla_{3D} \cdot \overline{u} \overline{S} + \nabla_{3D} \cdot \overline{u'S'}. \quad (3)$$

total mean eddy

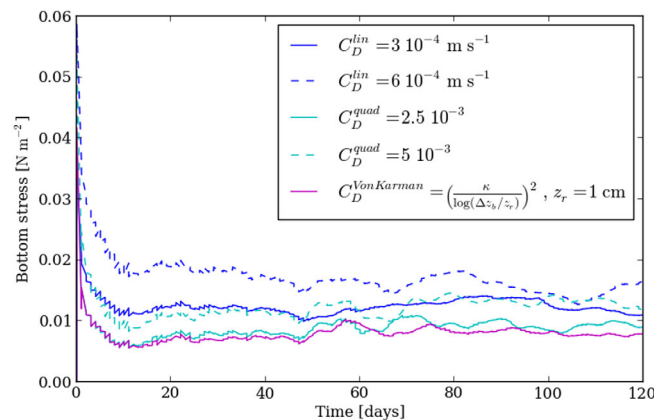


Figure 13. Horizontally integrated bottom stress as a function of time (120 days of simulation) with five different bottom stress parameterizations (see the legend for correspondence).

We average the *total* term computed online during 1 year, and compute offline the *mean* term from the averaged velocity and salinity fields. As such, we can estimate the *eddy* contribution as the difference between the total and the mean terms. In addition, contributions are vertically integrated over the salt tongue depth range (100–250 m). The first-order balance is between the mean and the eddy contributions, and the total advection term is weaker than both contributions. All other terms (mixing, rate, and forcing) are at least 1 order of magnitude smaller. As

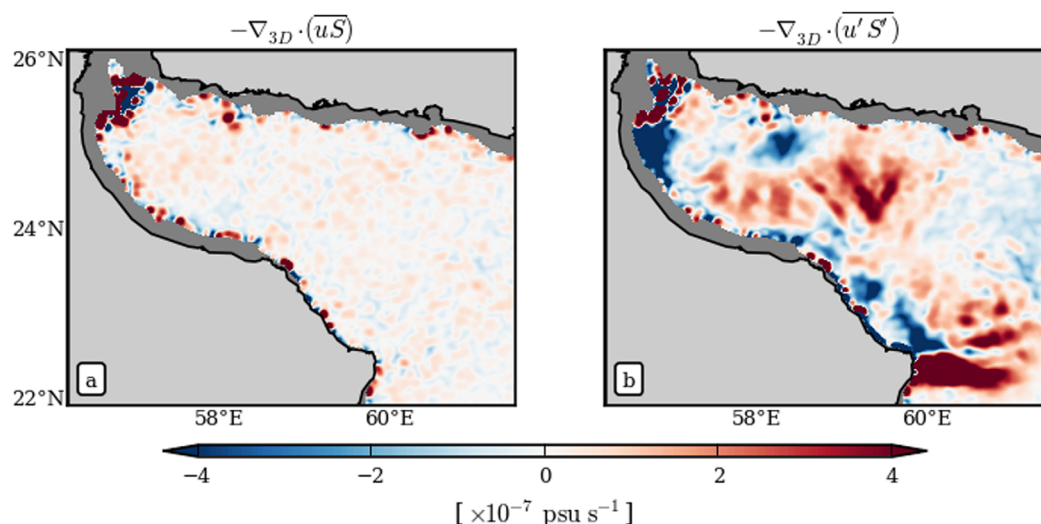


Figure 14. Convergence (i.e., minus divergence) of salt fluxes computed over 1 year and integrated between 100 and 250 m in the vertical. Figure 14a is the mean of total fluxes computed online and Figure 14b is the eddy salt flux divergence. Both fields have been spatially smoothed with a Gaussian filter of width 10 km.

such, we only show the total and the eddy terms in Figure 14 (the mean term is almost equal to the opposite of the eddy term). Displayed are opposite quantities of those in equation (3), i.e., convergence of fluxes. The most important contribution of eddy fluxes is done in the inner basin, where eddy fluxes contribute to the supply in salty waters (convergence of eddy fluxes). Values reach $\sim 2 \times 10^{-7} \text{ psu s}^{-1}$, i.e., $0.6 \text{ psu month}^{-1}$. Along the southern boundary, a dominance of negative convergence of eddy salt fluxes indicates that salt is *extracted* from the slope current at roughly similar rates. The role of eddy fluxes is thus to extract salinity from the boundaries (preferentially from the southern boundary where the slope current sits) and redistribute it in the interior of the Gulf. This provides a hint of explanation to understand how the almost isotropic salinity plume can form. In fact, the mean salinity gradient is directed in the along-gulf direction and the signature of the slope current is very weak (Figure 6a).

5.2. Lagrangian Perspective

We now examine synthetic particle trajectories released in the source of the outflow, in the Strait of Hormuz. This Lagrangian approach brings complementary information in terms of dispersion rate of particles during their journey through the Gulf of Oman which can under some assumptions and approximations be translated into eddy diffusivities (e.g., review on Lagrangian statistics in *LaCasce* [2008]). Particles are released off-line in the model solution, using the code described in *Gula et al.* [2014]. Neutrally buoyant particles are advected directly by the model velocity fields without any additional dispersion from the model's mixing processes. Model 12 hourly outputs are linearly interpolated in space and time. A time step of 7 min is chosen to respect the Friedrich-Courant-Levy condition imposed by $\Delta x = 2 \text{ km}$ and maximum model velocities of 1.8 m s^{-1} . A total of 120,000 particles are continuously injected in the outflow during 2 years to cover seasonal variations.

The mean trajectory of all released particles, i.e., the trajectory of their center of mass, is shown in Figure 15a. The trajectory is well centered in the cross-Gulf direction, from their release in the Strait until reaching the middle of the Gulf. This confirms the insignificant role played by the slope current. Examining an animation of their pathways confirms the role of mesoscale eddies in stirring them, northward (southward) when a cyclone (anticyclone) occupies the end of the Gulf.

On average, the PGW salt anomalies are diluted as they are transported toward the mouth of the Gulf. This is noticeable in particle's mean salinity (Figure 15a). To quantify this diffusion, we compute the absolute dispersion of particles around their mean position, that is, the mean square distance between particles and their center of mass $\langle d^2(t) \rangle$ at a function of time t , relative to the release absolute time ($\langle \cdot \rangle$ denotes an ensemble average). It reveals how a cloud of tracer spreads about its center of mass [*LaCasce*, 2008]. Figure 15b shows the dispersion evolution, computed with all particles released in the Strait. Three regimes are

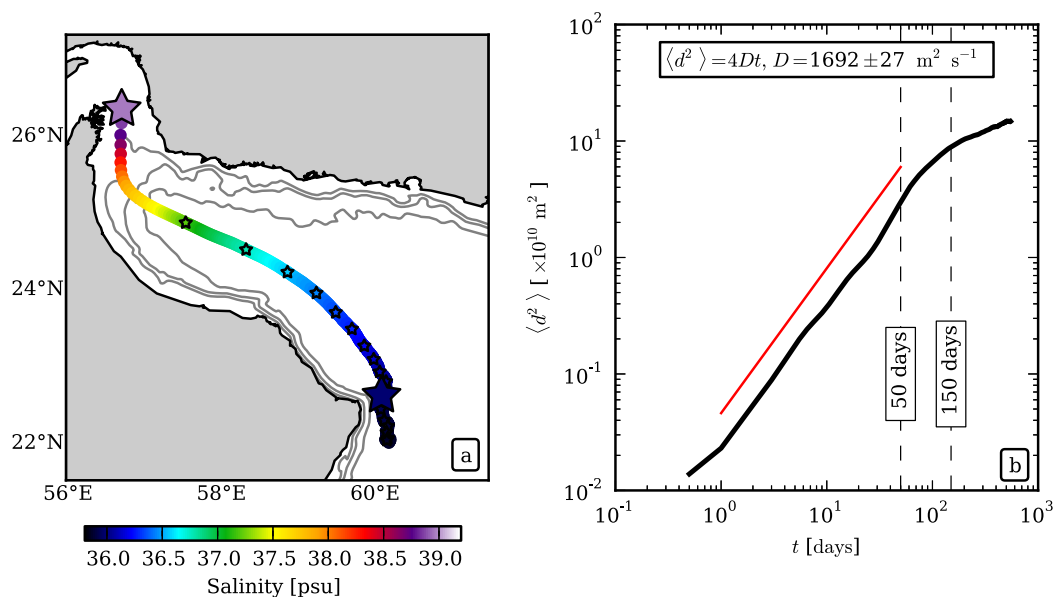


Figure 15. (a) Trajectory of the center of mass of 120,000 particles released in the outflow in the Strait of Hormuz during 2 years. There is one point per day, one small star every month, and one big star every year. Color is the mean salinity of the particles and isobaths 100, 250, and 1000 m are shown in gray lines. (b) Relative dispersion of particles relative to the center of mass as a function of time (black line) and linear regression computed between days 1 and 50 (red line). Correlation coefficient for linear fit is 0.98.

noticeable. First, from the release time to about 50 days, $\langle d^2(t) \rangle$ can be approximated by a linear function. $\langle d^2(t) \rangle \propto t$ suggests a diffusive behavior typical of a *random walk* process (same behavior was found in the surface and subsurface North Atlantic) [Colin de Verdière, 1983; LaCasce and Bower, 2000]. In a two-dimensional flow, in case of a linear dispersion, one can infer a diffusivity D :

$$\langle d^2(t) \rangle = 4Dt. \quad (4)$$

Assuming this model is valid and using a linear regression, we obtain a diffusivity $D = 1692 \pm 27 \text{ m}^2 \text{ s}^{-1}$. This value accounts for a variety of 3-D dispersive processes. Excluding particles whose depth evolution deviates from that of the center of mass by more than $\pm d_0$ a priori leads to a lower value D_{d_0} . For small d_0 this estimate should be more directly comparable to classical quasi-2-D isopycnal diffusivity values because the influence of dispersive processes in the vertical direction is limited. For $d_0 = 50 \text{ m}$, we find $D_{d_0} \sim 1600 \text{ m}^2 \text{ s}^{-1}$ which is still large and comparable to those obtained for well-known highly diffusive environments, e.g., in the Antarctic Circumpolar Current (ACC). For comparison, Abernathy *et al.* [2010] find values reaching $\sim 2000 \text{ m}^2 \text{ s}^{-1}$ in the ACC (although the method is different, it is also representative of an eddy diffusivity) whereas Colas *et al.* [2013] obtain $300\text{--}750 \text{ m}^2 \text{ s}^{-1}$ in an eastern boundary regime (California Current System). Note that this diffusivity corresponds to the dispersion during almost the first 2 months (50 days, until the second star in Figure 15a). A slight deep is visible in the dispersion curve after $t \sim 20$ days. It is due to a saturation of the across-gulf dispersion (not shown) component that is consistent with the elongated shape of the gulf. A transition occurs at 50 days, which corresponds to a standard deviation of $\sim 170 \text{ km}$ of the particle distance to the center of mass. This makes a disk of diameter 340 km that fills the Gulf.

Between days 50–150, there is a second stage, which is subdiffusive ($\langle d^2 \rangle \sim t^\alpha$, $\alpha < 1$). As the majority of the particles fill the Gulf, their overall dispersion is slowed down in the cross-Gulf direction (dispersion is anisotropic due to the Gulf geometry, not shown). A transition occurs around 150 days and marks the beginning of a third stage, which is associated with an even slower dispersion (i.e., smaller diffusivities). We hesitate to dynamically interpret this regime during which particles progressively exit the computational domain.

6. Summary

The realistic simulation evidences the important role of mesoscale eddies in spreading PGW in the Gulf of Oman at seasonal time scales, similarly to the fate of the Red Sea outflow in the Gulf of

Aden [Jlicak *et al.*, 2011]. Unlike in many other outflows, the slope current (along the southern coast) associated with outflowing waters is very intermittent and not instrumental in generating turbulence. The idealized simulations isolate the interaction of mesoscale eddies with the topography and reveal an enstrophy source at depth, located on the continental slope, that is produced by frictional effects in boundary layers. Friction is responsible for the formation of intense relative vorticity strips that detach from the continental slope and rapidly roll up into SCVs produced by instability. It is found in the realistic simulation that these SCVs trap PGW in their vicinity and contribute to PGW advection in the interior of the Gulf of Oman. SCVs are advected along the edges of the surrounding mesoscale eddies and do not live longer than 10 days due to the strong deformation rates there. Overall, this combination of processes mixes the salt input associated with PGW and produces a smooth large-scale salinity gradient in the Gulf. A release of virtual particles in the realistic simulation allowed to infer a diffusive regime with an estimated eddy diffusivity of $\sim 1700 \text{ m}^2 \text{ s}^{-1}$, typical of highly turbulent and dispersive regimes. This study thus brings an additional dynamical ingredient to the observations in L'Hégaret *et al.* [2013]: PGW in the interior of the basin is partly contained into SCVs that participate actively to its spreading.

Furthermore, we suggest that eddy-topography interactions creating submesoscale structures may often occur on continental slopes. Water masses trapped into SCVs may be spread into inner basins (away from boundaries) through this mechanism of transport. Eddy-topography interactions may well be a frequent and important process along continental slopes and contribute to offshore advection, dispersion and mixing of slope current waters in many other ocean sectors. For instance, recent fine-scale measurements by gliders in the Mediterranean Sea revealed the importance of SCVs, generated on the continental slope, to spread Levantine Intermediate Waters [Bosse *et al.*, 2015]. It is likely that the formation of SCVs by boundary layer detachment is not a rare process in the ocean. However, it is hard to observe because it is essentially a submesoscale process.

A step further in the study of the PGW spreading should be to focus on diabatic processes, especially on vertical mixing during the adjustment phase and horizontal mixing associated with SCVs collapse. The contribution of near Strait turbulence generated by pulses in the outflow could also lead to a richer variability in the spreading of PGW.

Acknowledgments

Eddy Available Potential Energy data set was downloaded from <http://stockage.univ-brest.fr/~rouillet/research.html>. MODIS SST data are available (Level 2) at <http://oceancolor.gsfc.nasa.gov/cgi/browse.pl>. SRTM30-plus bathymetry data set is available at http://topex.ucsd.edu/www_html/srtm30_plus.html. The altimeter products were produced by Ssalto/Duacs and distributed by Aviso, with support from Cnes (<http://www.aviso.altimetry.fr/duacs/>). CV is supported by the Direction Générale de l'Armement (DGA) and the Région Bretagne in the form of a PhD scholarship. C.V. benefited from a mobility grant from LABEX-MER to do an internship at UCLA. This study is a contribution to the French ANR Synbios. We thank two anonymous reviewers for their constructive remarks.

References

- Abernathy, R., J. Marshall, M. Mazloff, and E. Shuckburgh (2010), Enhancement of mesoscale eddy stirring at steering levels in the Southern Ocean, *J. Phys. Oceanogr.*, *40*(1), 170–184, doi:10.1175/2009JPO4201.1.
- Akueteve, C., and A. Wirth (2015), Dynamics of turbulent western-boundary currents at low latitude in a shallow-water model, *Ocean Sci.*, *11*(3), 471–481, doi:10.5194/os-11-471-2015.
- Banase, K. (1997), Irregular flow of Persian (Arabian) Gulf water to the Arabian Sea, *J. Mar. Res.*, *55*(6), 1049–1067, doi:10.1357/0022240973224120.
- Becker, J., et al. (2009), Global bathymetry and elevation data at 30 arc seconds resolution: SRTM30_PLUS, *Mar. Geod.*, *32*(4), 355–371.
- Böhm, E., J. Morrison, V. Manghnani, H. Kim, and C. Flagg (1999), The Ras al Hadd Jet: Remotely sensed and acoustic Doppler current profiler observations in 1994–1995, *Deep Sea Res., Part II*, *46*(8), 1531–1549, doi:10.1016/S0967-0645(99)00034-X.
- Bosse, A., P. Testor, L. Mortier, L. Prieur, V. Taillandier, F. d'Ortenzio, and L. Coppola (2015), Spreading of Levantine Intermediate Waters by submesoscale coherent vortices in the northwestern Mediterranean Sea as observed with gliders, *J. Geophys. Res. Oceans*, *120*, 1599–1622, doi:10.1002/2014JC010263.
- Bower, A. S., and H. H. Furey (2012), Mesoscale eddies in the Gulf of Aden and their impact on the spreading of Red Sea Outflow Water, *Prog. Oceanogr.*, *96*(1), 14–39, doi:10.1016/j.pocean.2011.09.003.
- Bower, A. S., H. D. Hunt, and J. F. Price (2000), Character and dynamics of the Red Sea and Persian Gulf outflows, *J. Geophys. Res.*, *105*(C3), 6387–6414, doi:10.1029/1999JC900297.
- Capet, X., F. Colas, J. McWilliams, P. Penven, and P. Marchesiello (2008), Eddies in eastern boundary subtropical upwelling systems, in *Ocean Modeling in an Eddying Regime*, *Geophys. Monogr. Ser.*, edited by M. W. Hecht and H. Hasumi, pp. 131–147, AGU, Washington, D. C.
- Carton, X., P. L'Hégaret, and R. Baraille (2012), Mesoscale variability of water masses in the Arabian Sea as revealed by ARGO floats, *Ocean Sci.*, *8*, 227–248, doi:10.5194/os-8-227-2012.
- Colas, F., X. Capet, J. C. McWilliams, and Z. Li (2013), Mesoscale eddy buoyancy flux and eddy-induced circulation in Eastern Boundary Currents, *J. Phys. Oceanogr.*, *43*(6), 1073–1095, doi:10.1175/JPO-D-11-0241.1.
- Colin de Verdière, A. (1983), Lagrangian eddy statistics from surface drifters in the eastern North Atlantic, *J. Mar. Res.*, *41*(3), 375–398.
- D'Asaro, E. A. (1988), Generation of submesoscale vortices: A new mechanism, *J. Geophys. Res.*, *93*(C6), 6685–6693.
- Dewar, W., J. McWilliams, and J. Molemaker (2015), Centrifugal instability and mixing in the California Undercurrent, *J. Phys. Oceanogr.*, *45*(5), 1224–1241, doi:10.1175/JPO-D-13-0269.1.
- Dong, C., J. C. McWilliams, and A. F. Shchepetkin (2007), Island wakes in deep water, *J. Phys. Oceanogr.*, *37*(4), 962–981, doi:10.1175/JPO3047.1.
- Frolow, S., G. Sutyrin, G. Rowe, and L. Rothstein (2004), Loop current eddy interaction with the western boundary in the Gulf of Mexico, *J. Phys. Oceanogr.*, *34*(10), 2223–2237, doi:10.1175/1520-0485(2004)034<2223:LCEIWT>2.0.CO;2.
- Griffiths, R. (1986), Gravity currents in rotating systems, *Annu. Rev. Fluid Mech.*, *18*(1), 59–89.

- Gula, J., M. J. Molemaker, and J. C. McWilliams (2014), Submesoscale cold filaments in the Gulf Stream, *J. Phys. Oceanogr.*, *44*(10), 2617–2643, doi:10.1175/JPO-D-14-0029.1.
- Gula, J., M. J. Molemaker, and J. C. McWilliams (2015), Topographic vorticity generation, submesoscale instability and vortex street formation in the Gulf Stream, *Geophys. Res. Lett.*, *42*, 4054–4062, doi:10.1002/2015GL063731.
- Ilicak, M., T. M. Özgökmen, and W. E. Johns (2011), How does the Red Sea outflow water interact with Gulf of Aden Eddies?, *Ocean Modell.*, *36*(1), 133–148, doi:10.1016/j.ocemod.2010.10.006.
- Johns, W., F. Yao, D. Olson, S. Josey, J. Grist, and D. Smeed (2003), Observations of seasonal exchange through the straits of Hormuz and the inferred heat and freshwater budgets of the Persian Gulf, *J. Geophys. Res.*, *108*(C12), 3391, doi:10.1029/2003JC001881.
- Laanaia, N., A. Wirth, J.-M. Molines, B. Barnier, and J. Verron (2010), On the numerical resolution of the bottom layer in simulations of oceanic gravity currents, *Ocean Sci.*, *6*(2), 563–572, doi:10.5194/os-6-563-2010.
- LaCasce, J. (2008), Statistics from Lagrangian observations, *Prog. Oceanogr.*, *77*(1), 1–29, doi:10.1016/j.pocean.2008.02.002.
- LaCasce, J., and A. Bower (2000), Relative dispersion in the subsurface North Atlantic, *J. Mar. Res.*, *58*(6), 863–894, doi:10.1357/002224000763485737.
- Legg, S., et al. (2009), Improving oceanic overflow representation in climate models: The gravity current entrainment climate process team, *Bull. Am. Meteorol. Soc.*, *90*, 657–670, doi:10.1175/2008BAMS2667.1.
- Lemarié, F., J. Kurian, A. F. Shchepetkin, M. Jeroen Molemaker, F. Colas, and J. C. McWilliams (2012), Are there inescapable issues prohibiting the use of terrain-following coordinates in climate models?, *Ocean Modell.*, *42*, 57–79, doi:10.1016/j.ocemod.2011.11.007.
- L'Hégaret, P. (2015), Etude de la circulation de mésoéchelle et des sorties d'eaux du Golfe Persique dans l'Océan Indien Nord-Ouest, PhD thesis, Univ. de Bretagne Occidentale, Brest, France.
- L'Hégaret, P., L. Lacour, X. Carton, G. Roullet, R. Baraille, and S. Corréard (2013), A seasonal dipolar eddy near Ras Al Hamra (Sea of Oman), *Ocean Dyn.*, *63*, 633–659, doi:10.1007/s10236-013-0616-2.
- L'Hégaret, P., R. Duarte, X. Carton, C. Vic, D. Ciani, R. Baraille, and S. Corréard (2015), Mesoscale variability in the Arabian Sea from HYCOM model results and observations: Impact on the Persian Gulf Water path, *Ocean Sci.*, *11*, 667–693, doi:10.5194/os-11-667-2015.
- Mason, E., J. Molemaker, A. F. Shchepetkin, F. Colas, J. C. McWilliams, and P. Sangrà (2010), Procedures for offline grid nesting in regional ocean models, *Ocean Modell.*, *35*(1), 1–15, doi:10.1016/j.ocemod.2010.05.007.
- McWilliams, J. C. (1985), Submesoscale, coherent vortices in the ocean, *Rev. Geophys.*, *23*(2), 165–182.
- Molemaker, M. J., J. C. McWilliams, and W. K. Dewar (2015), Submesoscale instability and generation of mesoscale anticyclones near a separation of the California Undercurrent, *J. Phys. Oceanogr.*, *45*(3), 613–629, doi:10.1175/JPO-D-13-0225.1.
- Nof, D. (1983), The translation of isolated cold eddies on a sloping bottom, *Deep Sea Res., Part A*, *30*(2), 171–182.
- Oey, L.-Y., and H. Zhang (2004), The generation of subsurface cyclones and jets through eddy-slope interaction, *Cont. Shelf Res.*, *24*(18), 2109–2131, doi:10.1016/j.csr.2004.07.007.
- Peters, H., W. E. Johns, A. S. Bower, and D. M. Fratantoni (2005), Mixing and entrainment in the Red Sea outflow plume. Part I: Plume structure, *J. Phys. Oceanogr.*, *35*(5), 569–583, doi:10.1175/JPO2679.1.
- Pous, S., X. Carton, and P. Lazure (2004), Hydrology and circulation in the Strait of Hormuz and the Gulf of Oman—Results from the GOGP99 Experiment: 2. Gulf of Oman, *J. Geophys. Res.*, *109*, C12038, doi:10.1029/2003JC002146.
- Price, J. F., and M. O'Neil Baringer (1994), Outflows and deep water production by marginal seas, *Prog. Oceanogr.*, *33*(3), 161–200, doi:10.1016/0079-6611(94)90027-2.
- Reverdin, G., J.-C. Gascard, B. Le Cann, L. Prieur, M. Assenbaum, and P. Lherminier (2009), A long-lasting mode water vortex in the Northeast Atlantic Ocean, *J. Phys. Oceanogr.*, *39*(3), 536–558, doi:10.1175/2008JPO3970.1.
- Risien, C., and D. Chelton (2008), A global climatology of surface wind and wind stress fields from eight years of QuikSCAT scatterometer data, *J. Phys. Oceanogr.*, *38*(11), 2379–2413, doi:10.1175/2008JPO3881.1.
- Robinson, S. K. (1991), Coherent motions in the turbulent boundary layer, *Annu. Rev. Fluid Mech.*, *23*(1), 601–639.
- Roullet, G., X. Capet, and G. Maze (2014), Global interior eddy available potential energy diagnosed from Argo floats, *Geophys. Res. Lett.*, *41*, 1651–1656, doi:10.1002/2013GL059004.
- Senjyu, T., T. Ishimaru, M. Matsuyama, and Y. Koike (1998), High salinity lens from the Strait of Hormuz, in *Offshore Environment of the ROPME Sea Area After the War-Related Oil Spill*, edited by A. Otsuki, M. Y. Abdulaheem, and R. M. Reynolds, pp. 35–48, Terra Science Pub., Tokyo.
- Shchepetkin, A., and J. McWilliams (2005), The regional oceanic modeling system (ROMS): A split-explicit, free-surface, topography-following-coordinate oceanic model, *Ocean Modell.*, *9*(4), 347–404, doi:10.1016/j.ocemod.2004.08.002.
- Smith, W., and D. Sandwell (1997), Global sea floor topography from satellite altimetry and ship depth soundings, *Science*, *277*(5334), 1956–1962, doi:10.1126/science.277.5334.1956.
- Stephens, J. (1997), Linear stability analysis of a gravity current over topography, in *Double-Diffusive Processes: 1996 Summer Study Program in Geophysical Fluid Dynamics*, edited by S. Meacham, pp. 287–310, Woods Hole Oceanogr. Inst., Mass.
- Sutyrin, G. G., and R. Grimshaw (2010), The long-time interaction of an eddy with shelf topography, *Ocean Modell.*, *32*(1), 25–35, doi:10.1016/j.ocemod.2009.08.001.
- Thoppil, P. G., and P. J. Hogan (2009), On the mechanisms of episodic salinity outflow events in the Strait of Hormuz, *J. Phys. Oceanogr.*, *39*(6), 1340–1360, doi:10.1175/2008JPO3941.1.
- Vic, C., G. Roullet, X. Carton, and X. Capet (2014), Mesoscale dynamics in the Arabian Sea and a focus on the Great Whirl life cycle: A numerical investigation using ROMS, *J. Geophys. Res. Oceans*, *119*, 6422–6443, doi:10.1002/2014JC009857.
- Wei, J., and D.-P. Wang (2009), A three-dimensional model study of warm core ring interaction with continental shelf and slope, *Cont. Shelf Res.*, *29*(13), 1635–1642, doi:10.1016/j.csr.2009.05.009.
- Wirth, A. (2009), On the basic structure of oceanic gravity currents, *Ocean Dyn.*, *59*(4), 551–563, doi:10.1007/s10236-009-0202-9.
- Worley, S., S. Woodruff, R. Reynolds, S. Lubker, and N. Lott (2005), ICOADS release 2.1 data and products, *Int. J. Climatol.*, *25*(7), 823–842, doi:10.1002/joc.1166.